HCl reaction decreases the $ClONO_2$ reaction depth slightly. The contribution of the HCl reaction increases in more dilute stratospheric aerosol because of the strong increase in the HCl solubility (19).

REFERENCES AND NOTES

1. S. Solomon, Nature 347, 347 (1990); "Scientific assessment of ozone depletion: 1991" (WMO Rep. 25, World Meteorological Society, Geneva, 1991).
2. D. J. Hofmann and S. Solomon, J. Geophys. Res. 94, 5029 (1989).
3. D. R. Hanson, A. R. Ravishankara, S. Solomon, ibid. 99, 3615 (1994).
4. M. A. Tolbert, M. J. Rossi, D. M. Golden, Geophys. Res. Lett. 15, 847 (1988); M. J. Rossi, R. Malhotra, D. M. Golden, ibid. 14, 127 (1987).
5. D. R. Hanson and A. R. Ravishankara, J. Geophys. Res. 96, 17307 (1991).
6. _____, J. Phys. Chem. 98, 5728 (1994).
7. N. A. Fuchs and A. G. Sutugin, Highly Dispersed Aerosols (Ann Arbor Science, Ann Arbor, MI, 1970); A. Fried, B. E. Henry, J. G. Calvert, M. Mozurkewich, J. Geophys. Res. 99, 3517 (1994).
8. P. V. Danckwerts, Trans. Faraday Soc. 47, 1014 (1951).
9. S. E. Schwartz, in Chemistry of Multiphase Atmospheric Systems, W. Jaeschke, Ed. (NATO Advanced Study Institutes Series, Springer-Verlag, Berlin), (1986), vol. G6, p. 415.
10. D. R. Hanson and E. R. Lovejoy, Geophys. Res. Lett. 21, 2401 (1994); E. R. Lovejoy and D. R. Hanson, J. Phys. Chem., in press.
11. Typical carrier gas (N_2 or N_2-O_2) flow velocities in the reactor were 1 to 1.5 cm s^{-1} (pressure = 620 torr) and $[ClONO_2]_o$ ranged from 10^{12} to 10^{13} molecules per cubic centimeter. We determined the aerosol size distribution and the surface-area concentration by measuring the aerosol number density and the extinction of ultraviolet light (200 to 400 nm) by the aerosol. The aerosol is characterized by a log-normal radius distribution (10) given by

$$dN = \frac{N}{\sqrt{2\pi} \log s} \exp \left\{ \frac{-[\log(r_{pk}/r)]^2}{2(\log s)^2} \right\} d \log r$$

where N is the number of particles, r_{pk} is the peak radius, and s is the geometric standard deviation. The H_2SO_4 aerosol was generated by passing a portion of the carrier gas over hot concentrated H_2SO_4 and then into a cool region. The aerosol size was varied by changing the gas flow rate and the temperature of the liquid H_2SO_4. We adjusted the composition of the aerosol by passing the aerosol through a conditioner containing a 59.9% H_2SO_4 solution (by weight) held at the same temperature as the flow tube reactor. The conditioner was either a 35-cm-long cylindrical tube with an inside diameter of 3 cm half filled with the solution or a coiled (~0.5 cm inside diameter by 100 cm long) glass tube coated with the solution. On the basis of model calculations of the liquid-to-aerosol vapor transfer rate within the conditioners, the composition of the aerosol exiting the conditioners was within 1% (by weight) of the conditioner liquid composition. For the experiments with HCl, the carrier gas was bubbled through a 59.9% H_2SO_4 solution (by weight) doped with 7.8×10^{-4} M HCl, before mixing with the aerosol. The aerosol stream was then passed through the coiled conditioner, which was charged with the same solution as the bubbler. The conditioner and bubbler transferred both H_2O and HCl vapor to the aerosol and were maintained at the same temperature (± 1 K) as the reactor by circulating chilled methanol through their jackets.
12. R. L. Brown, J. Res. Natl. Bur. Stand. 83, 1 (1978); C. J. Howard, J. Phys. Chem. 83, 3 (1979).
13. The concentration of HCl in the aerosol in the reaction region of the flow reactor was about 15% less than the concentration in the aerosol added to the reactor because of loss by reaction with $ClONO_2$ in the mixing and flow-transition region.
14. In our experiments, [HCl] was $\approx 6.6 \times 10^{-4}$ M and

the activity of H_2O was ≈ 0.12 (that is, $[H_2O] \sim 6.4$ M). Therefore, the ratio of the second-order rate coefficient for $ClONO_2$ + HCl to that of $ClONO_2$ + H_2O is approximately 1.5×10^5, which is comparable to the ratio extracted from measurements at 202 K ($\sim 1 \times 10^5$) (6). We did not account for a possible surface reaction between HCl-Cl$^-$ and $ClONO_2$ (6). It is expected that the surface reaction will contribute <15% to the reactivity in these experiments. By using the measured ℓ value and an estimate of 1×10^{-6} cm^2 s^{-1} for the $ClONO_2$ diffusion constant, we derive estimates for the hydrolysis and HCl rate coefficients of 1×10^4 and 1.5×10^9 M^{-1} s^{-1}, respectively, for 60% H_2SO_4 at 250 K. The HCl rate coefficient is in the diffusion-limited regime.
15. J. I. Gmitro and T. Vermeulen, Am. Inst. Chem. Eng. J. 10, 740 (1964).
16. The results from the present study suggest that the

HCl reaction is diffusion-limited at 250 K in 60% H_2SO_4 solution [see (14)]. In this case, the rate coefficient is proportional to the product of the capture radius and the diffusion constant. If we assume that the capture radius for the Cl$^-$ + $ClONO_2$ reaction is independent of temperature, we calculate that ℓ is 0.03 μm for $ClONO_2$ hydrolysis in 60% H_2SO_4 at 202 K.
17. D. J. Hofmann, Science 248, 996 (1990).
18. H. M. Steele and P. Hamill, J. Atmos. Sci. 12, 517 (1981).
19. D. R. Hanson and A. R. Ravishankara, J. Phys. Chem. 97, 12309 (1993).
20. This work was supported by the National Oceanic and Atmospheric Administration Global and Climate Change Program.

Rapid Deformation of the South Flank of Kilauea Volcano, Hawaii

Susan Owen, Paul Segall, Jeff Freymueller, Asta Miklius, Roger Denlinger, Thóra Árnadóttir,* Maurice Sako, Roland Bürgmann

The south flank of Kilauea volcano has experienced two large [magnitude (M) 7.2 and M 6.1] earthquakes in the past two decades. Global Positioning System measurements conducted between 1990 and 1993 reveal seaward displacements of Kilauea's central south flank at rates of up to about 10 centimeters per year. In contrast, the northern side of the volcano and the distal ends of the south flank did not displace significantly. The observations can be explained by slip on a low-angle fault beneath the south flank combined with dilation deep within Kilauea's rift system, both at rates of at least 15 centimeters per year.

Kilauea volcano, on the island of Hawaii, presents a major seismic as well as volcanic hazard (1). A M 8 earthquake shook the region in 1868 (2). A M 7.2 earthquake in 1975 (3) and a M 6.1 quake in 1989 (4, 5) were caused by seaward motion on a subhorizontal fault that may coincide with the base of the volcanic edifice (6). Swarms of shallow earthquakes accompany intrusions of magma into either of Kilauea's two rift zones (Fig. 1), but these earthquakes are typically small (M ≤ 4) and nondestructive (7). Earthquakes south of the rift zones have focal depths of 5 to 13 km (7), leading some to suggest that slip occurs on multiple parallel faults (5). However, precise relative relocations place many of the earthquakes on a well-defined northward dipping fault (8). This result, combined with the fact that the larger events occur within a narrow depth range, suggests that there is a single low-

S. Owen, P. Segall, J. Freymueller, T. Árnadóttir, R. Bürgmann, Geophysics Department, Stanford University, Stanford, CA 94305, USA.
A. Miklius, R. Denlinger, M. Sako, U.S. Geological Survey, Hawaiian Volcano Observatory, HI 96718, USA.

*Present address: Department of Geology, Victoria University, Wellington, New Zealand.

angle fault zone 7 to 9 km beneath Kilauea's south flank.

The structure of the rift system at depths of more than a few kilometers is uncertain because few earthquakes occur below 5 km. This lack of seismicity might indicate that deformation is concentrated in the shallow rift system, or simply that elevated temperatures at depth inhibit brittle failure. Delaney and colleagues (9) suggested that subsidence observed on leveling lines across the rift zones was caused by steady dilation at depths of ~4 to 9 km. Dvorak and colleagues (10) argued that deep dilation is not required and that the data can be explained by episodic shallow intrusions in combination with slip on a low-angle fault at 6 km. Horizontal deformation measurements on the north flank could distinguish between competing models of south-flank and rift zone kinematics. Electronic distance measurements (EDM) required line-of-site visibility, so that it was previously not possible to measure baselines on the heavily forested north flank of Kilauea (11, 12). Furthermore, it was not possible to determine displacements relative to sites removed from active volcanism and seismicity. EDM data for the period 1983 to 1991 have been interpreted to show seaward motion of the

Table 1. Weighted root mean square (millimeters) GPS residuals in the north, the east, and vertically.

	1990	1992	1993
North	6.4	3.6	2.2
East	9.1	6.2	5.8
Vertical	21.4	8.2	8.4

Fig. 1. Topography of Kilauea volcano with artificial illumination from the northwest. Circles are earthquake epicenters (*M* greater than 2.0) for the time period October 1989 to August 1993. Shallow earthquakes (0 to 5 km) are shown in red. Intermediate depth events (5 to 15 km) are shown in purple. All events were recorded by the Hawaiian Volcano Observatory with at least 10 *P* wave arrival times and horizontal errors of less than 1 km. SC, summit caldera; ERZ, east rift zone; SWRZ, southwest rift zone; HP, Hilina Pali fault system; ML, Mauna Loa; LS, Loihi seamount; PS, Papa'u seamount; MB, Midslope Bench with closed topographic depressions; and LT, toe of the postulated landslide system. Also shown are the surface projections of the model dislocation surfaces (see Fig. 3).
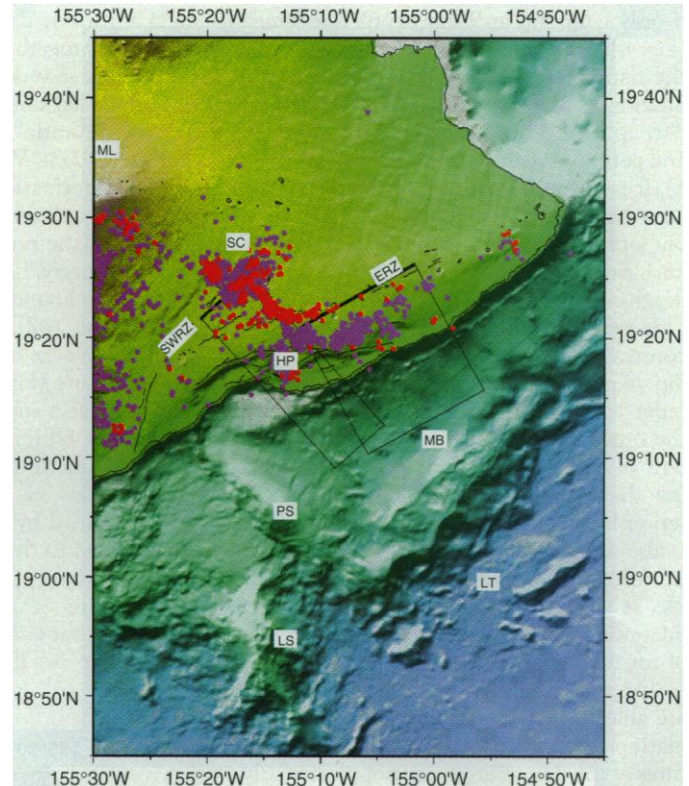

south flank (*13*); however, the network was geometrically weak and the data do not uniquely determine the velocity field (*14*). With the Global Positioning System (GPS), it is possible to determine three-dimensional displacements on both sides of the rift system with respect to a stable remote site (*15*).

GPS surveys were conducted on Kilauea in August and September 1990, February and March 1992, and August 1993 (*16*). In order to constrain the GPS satellite orbits, the 1990 and 1992 data were processed in 3- to 4-day orbital arcs (*17*), including data from between 3 and 10 permanent GPS sites in Hawaii, North America, and around the Pacific Rim. We fixed the coordinates of three fiducial sites to values determined from very long baseline interferometry (VLBI) (*18*) and then estimated satellite orbital parameters, the remaining station coordinates, tropospheric delay parameters, and integer cycle ambiguities (*19*). The 1993 ambiguity-fixed solutions used single-day orbital arcs and applied orbits determined by the International GPS Service (IGS) (*20*).

For each year, the individual multiday or daily solutions were combined with the use of a least-squares network adjustment. The resulting covariance matrices were scaled so that the residual sum of squares divided by the number of degrees of freedom equaled 1.0 (*21*). The residuals to the network adjustment provided a measure of data precision (Table 1). Average velocities for each station were calculated from the three annual solutions, with the assumption that the displacement rates are constant in time (*22*). Velocities were computed with respect to HP-6, a station on the island's stable northwest side (Fig. 2).

Our results (Fig. 2) show that the central south flank displaced horizontally at ~10 cm/year (11.7 ± 1.0 cm/year at M801 and 9.1 ± 0.3 cm/year at KAEN). Stations south of the east rift zone moved roughly perpendicular to the rift axis. The oblique motion of KALA may have been affected by the eruption at Pu'u O'o, only a few kilometers to the west. Stations near the southwest rift zone (SAND, KOAE, and KAMK) moved approximately perpendicular to the southwest rift axis. In contrast to the rapid velocities south of the rift zones, velocities north of the rifts were small or

insignificant. Even UWEK, on the northwest rim of the caldera, did not move horizontally. There are also steep gradients in velocity parallel to the rift system; velocities northeast of MOAN and southwest of KAMK are negligible. These gradients in velocity (strain rates) are dramatic. The extension rate across the caldera between UWEK and SAND, in a direction normal to the east rift zone, is ~15 microstrains per year. The average extension rate across the east rift zone between FERN and KMOA is ~5 microstrains per year. Locally, strain rates across the rift zone must be even higher. Extension rates across the rift system (for instance, HULU-GOAT and UWEK-SAND) are an order of magnitude greater than extension rates within the central south flank (for instance, PALI-APUA and GOAT-KAPU). One baseline, M801-KAEN, appears to have contracted, although the velocity of M801 is poorly determined. Velocity gradients parallel to the rift system (shear strain rates) are also large, averaging about 4 microstrains per year for the baselines HEIH-66YY and MOAN-66YY. In contrast, the maximum strain rates on the San Andreas fault are on the order of 0.3 microstrains per year (*23*).

Only four stations exhibited vertical displacement rates that were significant at two standard deviations: KALA, UWEK, HULU, and HEIH (Fig. 2). All are situated

in or near the rift-caldera system, and three (UWEK, HULU, and HEIH) subsided during the observation period. The fourth station, KALA, uplifted during the observation period, presumably in response to the nearby Pu'u O'o vent. The three rapidly moving coastal stations (APUA, KAEN, and KMOA) uplifted at an average rate of 0.8 ± 1.3 cm/year. This result is consistent with tide gauge measurements at APUA that show uplift of 2.1 ± 0.4 cm/year (*13*) between 1984 and 1991.

The fault beneath the south flank was modeled by two horizontal planes of shear dislocation in a homogeneous elastic half-space (*24*), with slip normal to the middle east rift zone. We modeled the rifts with three opening dislocations positioned along the rift zones (Fig. 3). We set the depth of the fault plane (D) at 9 km, consistent with the seismic data discussed above, and adjusted the other parameters to fit the GPS data. The resulting model (Fig. 3) shows that the dilating rift zones extend from a depth (*d*) of 1 to 3 km down to the fault plane at 9 km. The fault slip rate and rift dilation rate are both 20 cm/year, except along the upper east rift zone where the rift dilation rate is 10 cm/year. In comparison, the average slip rate on the San Andreas fault is only 3.5 cm/year.

The steep velocity gradients across the rift zones make it impossible to fit the data

if only fault slip at 9 km depth is assumed (Fig. 4). Rift dilation alone also cannot fit the data. A combination of fault slip and dilation of the rift zone at depth effectively decouples the south flank at the rift axes and permits a reasonable fit to the data (Fig. 3). It is possible to fit the observed gradient across the rift zones without rift dilation, but only if the fault is very shallow (~3 km). Such a model is inconsistent with the depths of major south flank earthquakes. Other model parameters are reasonably well constrained by the GPS observations. The dip of the fault must be subhorizontal in order to fit the modest coastal uplift. On the other hand, increasing the offshore extent of the fault and concurrently decreasing the slip rate to 15 cm/year does not seriously degrade the fit to the data. There is also a trade off between the height of the rift and the rate of rift opening. For example, it is possible to fit the data with rift dilation extending from 4 to 9 km if the rate of rift dilation is ~30 cm/year.

Despite the simplicity of the model, we are able to fit the overall pattern of deformation reasonably well. Some detailed features of the deformation are not particularly well fit, presumably due to the fact that the model does not include a summit magma chamber, the Koae fault zone (25), the Hilina Pali fault system, the Pu'u O'o vent, or an accurate representation of the rift system geometry. The stations with the largest misfit are KALA, which is probably affected by the Pu'u O'o eruption, and HULU, which is located within the upper east rift zone and is strongly influenced by local deformation. The model predicts vertical displacement rates that are less than measurement uncertainties for most stations. This is consistent with the lack of significant vertical motion observed outside the rift zones.

The model fault planes correspond well with the distribution of south flank seismicity from 1990 to 1993 (Fig. 1) and with the source area of the 1975 earthquake (12). During this time period, however, the cumulative seismic moment of south flank earthquakes and the magnitude of shallow rift intrusions are too small to account for the measured displacements. Thus, the observed motions are neither a direct result of current south flank microseismicity nor of episodic rift intrusion.

It has been proposed that the Hilina Pali normal faults (Fig. 1) are the headwall scarps of a giant landslide (26). There is evidence from wave deposits and from side-scan sonar data that older Hawaiian volcanoes have collapsed in catastrophic landslides (27, 28). A series of closed basins offshore of the Hilina Palis (29) (Fig. 1) must be young, because the high influx of volcanic sediments from Kilauea would

quickly fill any depression (30). These observations, together with the high rates of south flank seismicity (Fig. 1) and deformation, have led some to suggest that Kilauea has the potential to fail in a catastrophic landslide (27). We observed the highest rates of deformation where the Hilina Pali faults are well expressed (Fig. 2). Papa'u Seamount, the prominent linear feature in the bathymetry, has been suggested to form the western boundary of a Hilina megaland-slide system (27). However, we find that the western edge of the modeled fault is east of this feature (Fig. 1). The eastern edge is located near a small right step in the east rift zone at HEIH but does not correspond to a prominent bathymetric feature. The seaward edge of the basal fault plane is poorly defined by the GPS data and could be extended to the postulated landslide toe without seriously degrading the data fit. We are unaware of any evidence for lateral "tear" faults at either the eastern or western edges of the rapidly deforming zones, which

suggests that the deformation pattern has varied over time.

The GPS data allow us to distinguish between the two competing models for rift zone subsidence discussed above. A consequence of Delaney and colleagues' model of deep rift dilation (9) is a decoupling of the south flank, which we have shown clearly exists in the GPS results (Fig. 2). Dilation of the rift zones also has implications for the volcano's magma supply budget. The dislocation model presented here implies a 0.06 km^3/year volume increase due to rift dilatation. This is roughly 60% of the long-term magma supply rate as determined from the accumulation of lavas and estimated changes in summit magma chamber volume (31), which demonstrates that rift zone dilation must be accounted for when computing magma supply rate.

The dislocation model is merely kinematic, and although it puts constraints on mechanical processes at work in Kilauea, it
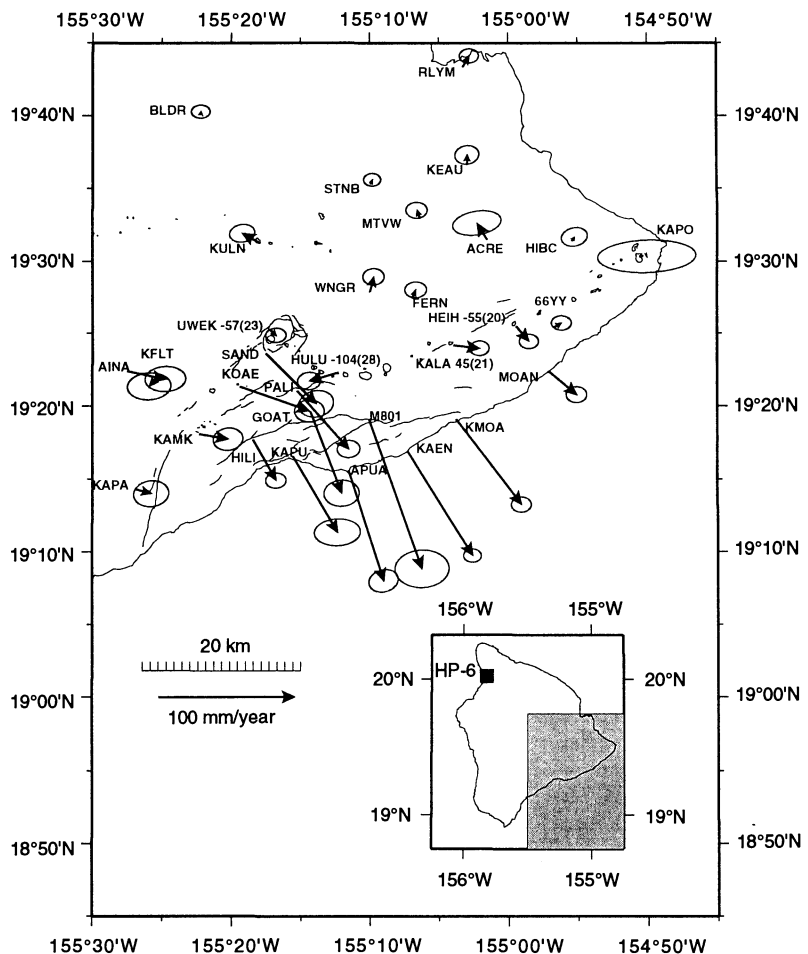

Fig. 2. Average horizontal velocities determined from GPS surveys computed relative to HP-6 on the northwest side of the island of Hawaii (see inset). Ellipses represent 95% confidence intervals. The size of the error ellipses varies depending on the amount of data collected at each site. Velocities of stations not observed in 1990 have greater uncertainty. Average vertical displacement rates (in millimeters per year) with 1-sigma uncertainties are shown next to the four-character station codes only for sites where the vertical motions are significant at the 2-sigma level.

1330

does not directly address the forces driving deformation (32). It has been postulated that gravitational spreading of dense residual melts (33) or dunite cumulates (34) may drive south flank motion. It has also been suggested that high fluid pressures in abyssal sediments trapped beneath the volcano promote slip on the basal fault (35).

The absence of a tear fault near HEIH suggests that, over sufficiently long periods of time, the south flank adjacent to the lower east rift also displaces seaward, which may occur seismically. The greatest potential hazard associated with the south flank of Kilauea is probably a tsunami, which could effect the more populated areas of the Big Island or indeed other islands. These could range in size from the tsunami that accompanied the 1975 earthquake (36) to a much larger event if the south flank fails in a catastrophic landslide. Analysis of baseline length changes determined by geodimeters between 1970 and 1990 suggests that the present rate of south flank motion is not anomalously fast. The south flank was probably moving faster in the years after the 1975 earthquake. It is notable that as south flank seismicity decayed to background values (10), the rate of south flank motion presumably decreased to 10 cm/year. More frequent monitoring is needed to evaluate changes in deformation rates on Kilauea's unstable south flank.

Fig. 3. Comparison of observed horizontal velocities and those predicted by a simple dislocation model. Ellipses represent 95% confidence intervals. Surface projections of the horizontal dislocation surfaces are shown as shaded rectangles. The vertical dislocation surfaces that model the deep rift zones are indicated by heavy lines. The inset shows a cross section of the model geometry.
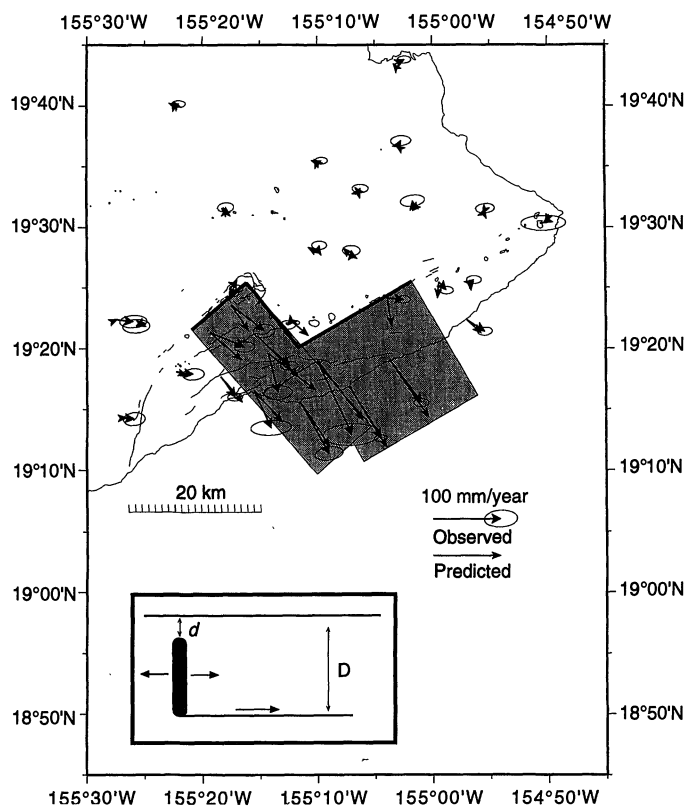
Fig. 4. Comparison of models. (**A**) Horizontal velocity (positive seaward). (**B**) Uplift rate. Profiles are parallel to the slip direction along the symmetry axis of the easternmost fault shown in Fig. 3. Data points with one standard deviation error bars are shown. Fault slip and rift opening rates in each model were adjusted to fit the horizontal velocity at KMOA. Fault only: Fault slip, at 43 cm/year, on a horizontal fault at a depth of 9 km. Rift only: Dilation in a vertical rift zone, at 37 cm/year, at a depth of 2 to 9 km. Fault and rift: 20

cm/year slip on a horizontal fault at a depth of 9 km and 20 cm/year dilation on a vertical rift at a depth of 2 to 9 km. Fault slip alone causes stations north of the rift to move seaward and generates a broad zone of subsidence, both of which are inconsistent with the data. Dilation of the rift system alone causes stations north of the rift to move inland and uplifts the rift flanks, which is also inconsistent with the data. Slip on the basal fault combined with deep dilation of the rift system, however, predicts rapid seaward motion south of the rift, negligible motions north of the rift, and a narrow zone of subsidence centered on the rift—all features that are observed in the data.
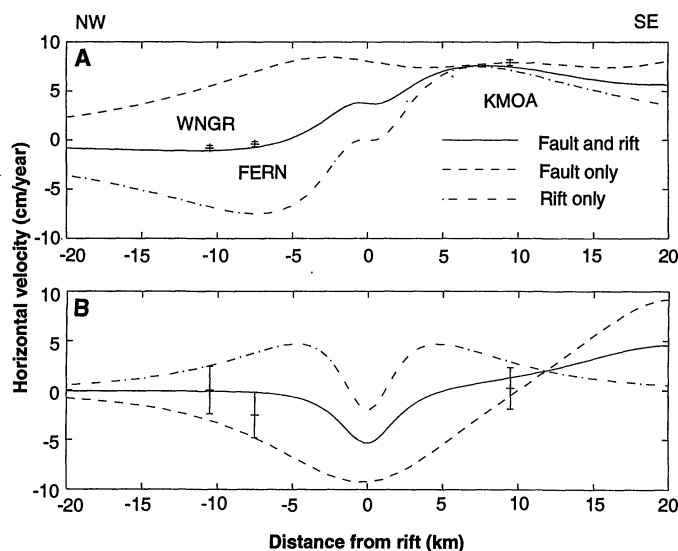
REFERENCES AND NOTES

1. R. I. Tilling and J. J. Dvorak, *Nature* **363**, 125 (1993).
2. M. Wyss, *Bull. Seismol. Soc. Am.* **78**, 1450 (1988).
3. M. Ando, *J. Geophys. Res.* **84**, 7616 (1979); H. K. Eissler and H. Kanamori, *ibid.* **92**, 4827 (1987).
4. T. Árnadóttir, P. Segall, P. Delaney, *Geophys. Res. Lett.* **18**, 2217 (1991); C. J. Bryan, *Bull. Seismol. Soc. Am.* **82**, 2368 (1992).
5. J. Dvorak, *J. Geophys. Res.* **99**, 9533 (1994).
6. A. S. Furumoto and R. L. Kovach, *Phys. Earth Planet. Inter.* **18**, 197 (1979); R. S. Crosson and E. T. Endo, *Bull. Seismol. Soc. Am.* **71**, 713 (1981); C. H. Thurber and A. E. Gripp, *J. Geophys. Res.* **93**, 4271 (1988).
7. F. W. Klein, R. Y. Koyanagi, J. S. Nakata, W. R. Tanigawa, *U.S. Geol. Surv. Prof. Pap.* **1350**, 1019 (1987).
8. J.-L. Got, J. Frechet, F. W. Klein, *J. Geophys. Res.* **99**, 15375 (1994).
9. P. T. Delaney, R. S. Fiske, A. Miklius, A. T. Okamura, M. K. Sako, *Science* **247**, 1311 (1990).
10. J. J. Dvorak, F. W. Klein, D. A. Swanson, *Bull. Seismol. Soc. Am.* **84**, 133 (1994).
11. D. A. Swanson, W. A. Duffield, R. S. Fiske, *U.S. Geol. Surv. Prof. Pap.* **963**, 1 (1976).
12. P. W. Lipman, J. P. Lockwood, R. G. Okamura, D. A. Swanson, K. M. Yamashita, *U.S. Geol. Surv. Prof. Pap.* **1276**, 1 (1985).
13. P. T. Delaney, A. Miklius, T. Árnadóttir, A. T. Okamura, M. K. Sako, *J. Geophys. Res.* **98**, 17801 (1993).
14. Repeated distance measurements do not constrain rigid body translations and rotations of the network. The 1983–1991 trilateration network also contained network defects that make it impossible to uniquely resolve station velocities. Delaney and colleagues (13) used a "model coordinate solution" [P. Segall and M. V. Matthews, *J. Geophys. Res.* **93**, 14954 (1988)] in which the unresolved components of the displacement field were constrained by an assumed model of the deformation.
15. J. J. Dvorak, A. T. Okamura, M. Lisowski, W. Prescott, J. Svarc, *Eos* **73**, 118 (1992); P. Segall, P. Delaney, T. Árnadóttir, J. Freymueller, S. Owen, *ibid.*, p. 505; J. J. Dvorak, A. T. Okamura, M. Lisowski, W. Prescott, J. Svarc, *U.S. Geol. Surv. Bull.* **2092** (1994).
16. The 1990 survey used TI-4100 and Trimble SST receivers. Trimble SST and Ashtech LD-XII and MD-XII receivers were used in 1992; Ashtech P-12 and Trimble SSE and SST receivers were used in 1993. The TI-4100, Ashtech P-12, and Trimble SSE receivers record dual frequency P-code and phase data; the other receivers record single frequency C/A code and dual-frequency phase data.
17. J. L. Davis, W. H. Prescott, J. L. Svarc, K. J. Wendt, *J. Geophys. Res.* **94**, 13635 (1989). The 1990 and 1992 data were analyzed with Bernese 3.3 software. M. Rothacher, G. Beutler, W. Gurtner, T. Schildknecht, U. Wild, documentation for Bernese GPS

Software Version 3.2 (University of Bern, Bern, Switzerland, 1990); G. Beutler, I. Bauersima, W. Gurtner, M. Rothacher, T. Schildknecht, in *Lecture Notes in Earth Sciences*, E. Groten and R. Strauss, Eds. (Springer-Verlag, New York, 1988), pp. 363–380.

18. Goddard Space Flight Center VLBI model GLB 753, C. Ma, J. Ryan, D. S. Caprette, NASA Technical Memorandum 104552.

19. We were able to resolve nearly all of the integer cycle ambiguities in 1992 and a significant number in 1990. Ambiguity resolution was not uniformly successful on baselines longer than 50 km or for which there was less than 6 hours of data.

20. G. Beutler, P. Morgan, R. E. Neilan, *GPS World* (February, 1993), p. 40. The 1993 data were reduced with GIPSY software. S. M. Lichten and J. S. Border, *J. Geophys. Res.* **92**, 12751 (1987); S. M. Lichten, *Manuscripta Geodetica* **15**, 159 (1990). We included data from seven global tracking stations to tie the Hawaii network to the IGS reference frame.

21. This procedure is conservative in that it treats any actual deformation occurring during the annual surveys as measurement error.

22. Only two stations are inconsistent with the constant rate model. One of these, HULU, is located within the upper east rift zone and may have been affected by local deformation. We suspect a problem in the 1992 data at the second site, KULN.

23. W. Thatcher, *U.S. Geol. Surv. Prof. Pap.* **1515**, 189 (1990).

24. Y. Okada, *Bull. Seismol. Soc. Am.* **75**, 1135 (1985).

25. W. A. Duffield, *U.S. Geol. Surv. Prof. Pap.* **856**, 1 (1975).

26. H. T. Stearns and W. O. Clark, *U.S. Geol. Surv. Water-Supply Paper 616*, 194 (1930); H. T. Stearns and G. A. MacDonald, *Hawaii Div. Hydrograph. Bull.* **9**, 363 (1946); J. G. Moore and H. L. Krivoy, *J. Geophys. Res.* **69**, 2033 (1964).

27. P. W. Lipman, W. R. Normark, J. G. Moore, J. B. Wilson, C. E. Gutmacher, *J. Geophys. Res.* **93**, 4279 (1988).

28. J. G. Moore et al., ibid. **94**, 17465 (1989); J. G. Moore and G. W. Moore, *Science* **226**, 1312 (1984).

29. W. W. Chadwick et al., *U.S. Geol. Surv. Misc. Field Stud. Map MF-2231* (1993); J. R. Smith, Sheet 5, *Hawaii Seafloor Atlas* (Hawaii Institute of Geophysics and Planetology, Honolulu, HI, 1994).

30. J. R. Smith, *Eos* **73**, 507 (1992); W. W. Chadwick, J. G. Moore, C. G. Fox, D. M. Christie, ibid., p. 507.

31. D. A. Swanson, *Science* **175**, 169 (1972); D. Dzuri-sin, R. Y. Koyanagi, T. T. English, *J. Volcanol. Geotherm. Res.* **21**, 177 (1984).

32. J. H. Dieterich, *J. Geophys. Res.* **93**, 4258 (1988).

33. M. P. Ryan, ibid., p. 4213.

34. A. Borgia, ibid. **99**, 17791 (1994); D. A. Clague and R. P. Denlinger, in preparation.

35. K. Nakamura, *Bull. Volcanol. Soc. Jpn.* **25**, 255 (1980).

36. D. C. Cox, *Source of the Tsunami Associated with the Kalapana (Hawaii) Earthquake of November 1975* (Hawaii Institute of Geophysics, Honolulu, HI, 1980).

37. The August 1990 GPS data were collected under the supervision of J. Dvorak. Thanks to V. Smith, L. Liu, E. Yu, and A. Okamura for help in collecting the field data. P. Okubo provided the earthquake summary data shown in Fig. 1. J. Smith provided the digital topographic and bathymetric data in Fig. 1. Thanks to T. Duennebier for help with graphics and to Y. Bock for providing cleaned GPS tracking data for August 1990. Thanks to P. Delaney and D. Swanson for comments on an early draft of the manuscript.

9 September 1994; accepted 1 December 1994

Multilayer White Light–Emitting Organic Electroluminescent Device

Junji Kido, Masato Kimura, Katsutoshi Nagai

Organic electroluminescent devices are light-emitting diodes in which the active materials consist entirely of organic materials. Here, the fabrication of a white light–emitting organic electroluminescent device made from vacuum-deposited organic thin films is reported. In this device, three emitter layers with different carrier transport properties, each emitting blue, green, or red light, are used to generate white light. Bright white light, over 2000 candelas per square meter, nearly as bright as a fluorescent lamp, was successfully obtained at low drive voltages such as 15 to 16 volts. The applications of such a device include paper-thin light sources, which are particularly useful for places that require lightweight illumination devices, such as in aircraft and space shuttles. Other uses are a backlight for liquid crystal display as well as full color displays, achieved by combining the emitters with micropatterned color filters.

Electroluminescent (EL) devices based on organic thin layers are one of the most promising next-generation flat panel display systems. These devices can be made into large-area, extremely thin full color displays that can be operated by batteries. The structure of the devices is simple, having organic thin layers sandwiched between two electrodes. Because organic layers can be formed by vacuum evaporation or solution casting, the fabrication cost could be less than that of the liquid crystal displays, which are today the most widely used flat panel displays.

In organic EL devices, the generation of light is the consequence of the recombination of holes and electrons injected from the electrodes. Such carrier recombination in the organic emitter layer excites the emitting centers. In a chemical sense, the reaction of radical cations (holes) and radical anions (electrons) provides excited

Department of Materials Science and Engineering, Yamagata University, Yonezawa, Yamagata 992, Japan.

molecules that emit light as one of the decay processes. A variety of materials have been investigated as active materials (1–9), and a number of device structures (10–22) have been proposed because it is important to find an appropriate device structure to maximize the carrier recombination efficiency.

The use of multilayer structures was first demonstrated by Tang and VanSlyke (1). They used a hole-transport layer for hole injection from the electrode into the electron-transporting emitter layer, which significantly improved the EL efficiency to 1.5 lm/W. Bright electroluminescence of over 1000 cd/m², which is high enough for practical applications, with a voltage below 10 V was achieved first. Their device consisted of two active layers with an organic hole-transport layer and an electron-transporting luminescent metal complex layer. The hole-transport layer plays an important role not only in transporting holes but also in blocking electrons, thus preventing electrons from moving into the opposite elec-

trode without recombining with holes. The recombination, therefore, mainly takes place in the emitter layer. Since this first device, various types of EL devices with a multilayer structure have been reported. For instance, a luminescent hole-transporting material can also be an emitter layer when combined with an appropriate electron-transport layer (4, 9, 13).

In the above examples, various emitting colors have been obtained, including the three primary colors of blue, green, and red. However, there are few white light–emitting devices owing to the lack of the organic fluorescent dyes with white fluorescence. We have therefore focused on developing white light–emitting EL devices and have recently developed one made from a polymer emitter layer doped with three kinds of fluorescence dyes, each emitting blue, green, or red to produce white light (17).

In this study, we developed a device structure with three emitter layers, each emitting in the different region of the visible spectrum to generate white light. In general, organic EL devices are composed of two organic layers, each transporting either holes or electrons. In such a device, one of the two layers functions as an emitter layer and the other as a carrier transport layer. Therefore, the emission color is determined by the fluorescence properties of the emitter material, and the light is of the particular color of the emitting material.

One way to add another emission color to such a device is to dope the emitter layer with a fluorescent dye of a different color. For example, it was demonstrated that, in a device with an electron-transporting green-emitting aluminum chelate emitter and a hole-transport layer, when the chelate layer is partly doped with a red-emitting fluorescent dye, the resulting light becomes a mixture of the lights from the two emitter materials, thus producing yellow light (12).